A&A 553, A21 (2013)
DOI: 10.1051/0004-6361/201220797

Astronomy & Astrophysics

Spatial distribution of water in the stratosphere of Jupiter from *Herschel* HIFI and PACS observations⋆,⋆⋆

T. Cavalié[1,2], H. Feuchtgruber[3], E. Lellouch[4], M. de Val-Borro[5,6], C. Jarchow[5], R. Moreno[4], P. Hartogh[5], G. Orton[7], T. K. Greathouse[8], F. Billebaud[1,2], M. Dobrijevic[1,2], L. M. Lara[9], A. González[5,9], and H. Sagawa[10]

[1] Univ. Bordeaux, LAB, UMR 5804, 33270 Floirac, France
e-mail: cavalie@obs.u-bordeaux1.fr
[2] CNRS, LAB, UMR 5804, 33270 Floirac, France
[3] Max Planck Institut für Extraterrestrische Physik, 85741 Garching, Germany
[4] LESIA–Observatoire de Paris, CNRS, Université Paris 06, Université Paris–Diderot, 5 place Jules Janssen, 92195 Meudon, France
[5] Max Planck Institut für Sonnensystemforschung, 37191 Katlenburg-Lindau, Germany
[6] Department of Astrophysical Sciences, Princeton University, Princeton, NJ 08544, USA
[7] Jet Propulsion Laboratory, California Institute of Technology, CA 91109 Pasadena, USA
[8] Southwest Research Institute, San Antonio, TX 78228, USA
[9] Instituto de Astrofísica de Andalucía (CSIC), 18008 Granada, Spain
[10] National Institute of Information and Communications Technology, 4-2-1 Nukui-kita, Koganei, Tokyo 184-8795, Japan

Received 27 November 2012 / Accepted 13 February 2013

ABSTRACT

Context. In the past 15 years, several studies suggested that water in the stratosphere of Jupiter originated from the Shoemaker-Levy 9 (SL9) comet impacts in July 1994, but a direct proof was missing. Only a very sensitive instrument observing with high spectral/spatial resolution can help to solve this problem. This is the case of the *Herschel* Space Observatory, which is the first telescope capable of mapping water in Jupiter's stratosphere.
Aims. We observed the spatial distribution of the water emission in Jupiter's stratosphere with the Heterodyne Instrument for the Far Infrared (HIFI) and the Photodetector Array Camera and Spectrometer (PACS) onboard *Herschel* to constrain its origin. In parallel, we monitored Jupiter's stratospheric temperature with the NASA Infrared Telescope Facility (IRTF) to separate temperature from water variability.
Methods. We obtained a 25-point map of the 1669.9 GHz water line with HIFI in July 2010 and several maps with PACS in October 2009 and December 2010. The 2010 PACS map is a 400-point raster of the water 66.4 μm emission. Additionally, we mapped the methane ν_4 band emission to constrain the stratospheric temperature in Jupiter in the same periods with the IRTF.
Results. Water is found to be restricted to pressures lower than 2 mbar. Its column density decreases by a factor of 2–3 between southern and northern latitudes, consistently between the HIFI and the PACS 66.4 μm maps. We infer that an emission maximum seen around 15 °S is caused by a warm stratospheric belt detected in the IRTF data.
Conclusions. Latitudinal temperature variability cannot explain the global north-south asymmetry in the water maps. From the latitudinal and vertical distributions of water in Jupiter's stratosphere, we rule out interplanetary dust particles as its main source. Furthermore, we demonstrate that Jupiter's stratospheric water was delivered by the SL9 comet and that more than 95% of the observed water comes from the comet according to our models.

Key words. planets and satellites: individual: Jupiter – planets and satellites: atmospheres – submillimeter: planetary systems

1. Introduction

Thermochemistry, photochemistry, vertical and horizontal transport, condensation, and external supplies are the principal physico-chemical processes that govern the 3D distributions of oxygen compounds in giant planet atmospheres. There are several sources of external supply for oxygen material in the atmospheres of the outer planets: interplanetary dust particles (IDP; Prather et al. 1978), icy rings and satellites (Strobel & Yung 1979), and large comet impacts (Lellouch et al. 1995). The vertical and horizontal distributions of oxygen compounds are a diagnostic of their source(s). The temporal evolution of these distributions can also contain the signature of a given source, especially if sporadic (as in the case of a comet impact).

Water in the atmospheres of the outer planets has both an internal and an external source (e.g., Larson et al. 1975 and Lellouch et al. 2002 for Jupiter). These sources are separated by a condensation layer, the tropopause cold trap, which acts as a transport barrier between the troposphere and the stratosphere. Thus, the water vapor observed by the Infrared Space Observatory (ISO) in the stratosphere of the giant planets has an external origin (Feuchtgruber et al. 1997). While Saturn's water seems to be provided by the Enceladus torus (Hartogh et al. 2011), the water origin in Uranus and Neptune remains unclear. For Jupiter, IDP or the Shoemaker-Levy 9 (SL9) comet, which collided with the planet in July 1994 at 44 °S, are the main candidates (Landgraf et al. 2002; Bjoraker et al. 1996).

⋆ *Herschel* is an ESA space observatory with science instruments provided by European-led Principal Investigator consortia and with important participation from NASA.
⋆⋆ Figures 1 and 3 are available in electronic form at http://www.aanda.org

Several clues or indirect proofs have suggested a cometary origin for the source of external water in Jupiter. First, Lellouch et al. (2002) analyzed the water and carbon dioxide (CO_2) observations by ISO. They could only reconcile the short-wavelength spectrometer (SWS) and the long-wavelength spectrometer (LWS) water data by invoking an SL9 origin but failed at reproducing the Submillimeter Wave Astronomy Satellite (SWAS) observation with their water vertical profile. In parallel, they showed that the meridional distribution of CO_2, produced from the photochemistry of water, was a direct proof that CO_2 was produced from SL9 (higher abundance in the southern hemisphere). Then, the analysis of the SWAS and Odin space telescope observations seemed to indicate that the temporal evolution of the 556.9 GHz line of water was better modeled assuming the aftermath of a comet impact (Cavalié et al. 2008b, 2012). However, IDP models have never been completely ruled out by these studies because the signal-to-noise ratio (S/N) and/or spatial resolution were never quite good enough.

The reason why some doubts have remained on the source of water in Jupiter's stratosphere is in the first place the lack of observations prior to the SL9 impacts. Since then, the lack of very high S/N and spectrally/spatially resolved observations prevented differentiating the SL9 source from any other source. High-sensitivity observations in the (sub)millimeter and in the infrared have led to converging clues for carbon monoxide (CO), advocating for a regular delivery of oxygen material to the giant planet atmospheres by large comets (Bézard et al. 2002 and Moreno et al. 2003 for Jupiter; Cavalié et al. 2009, 2010 for Saturn; Lellouch et al. 2005, 2010 and Hesman et al. 2007 for Neptune). High-sensitivity (sub)millimeter line spectroscopy performed with the *Herschel* Space Observatory now offers the means to solve this problem for water. Indeed, the very high spectral resolution in heterodyne spectroscopy enables the retrieval of line profiles and thus vertical distributions, while the horizontal distributions can be recovered from observations carried out with sufficient spatial resolution. Obviously, temporal monitoring of these distributions can be achieved by repeating the measurements.

In this paper, we report the first high S/N spatially resolved mapping observations of water in Jupiter carried out with the ESA *Herschel* Space Observatory (Pilbratt et al. 2010) and its Heterodyne Instrument for the Far Infrared (HIFI; de Graauw et al. 2010) and Photodetector Array Camera and Spectrometer (PACS; Poglitsch et al. 2010) instruments. These observations have been obtained in the framework of the guaranteed time key program "Water and related chemistry in the solar system", also known as "*Herschel* solar system Observations" (HssO; Hartogh et al. 2009b). We also present spatially resolved IRTF observations of the methane ν_4 band, obtained concomitantly, to constrain the stratospheric temperature. In Sects. 2 and 3, we present the various Jupiter mapping observations and models we used to analyze the water maps. We describe our results on the distribution of water in Sect. 4 and discuss the origin of this species in Sect. 5 in view of these results. We finally give our conclusions in Sect. 6.

2. Observations

2.1. Herschel observations

2.1.1. *Herschel*/HIFI map

The HIFI mapping observation (Observation ID: 1342200757) was carried out on July 7, 2010, operational day (OD) 419, in dual beam switch mode (Roelfsema et al. 2012). We obtained a 5×5 pixels raster map with a $10''$ separation between pixels, that is, covering a region of $40'' \times 40''$, centered on Jupiter. More details are given in Table 1.

We targeted the water line at 1669.905 GHz (179.5 μm) with a half-power beam width of $12\farcs7$. Because of the fast rotation of Jupiter, the line is Doppler shifted. Because the bandwidth of the High Resolution Spectrometer (HRS) was too narrow to encompass the whole water line, we only used the Wide Band Spectrometer (WBS) data, whose native resolution is 1.1 MHz. We processed the data with the standard HIPE 8.2.0 pipeline (Ott 2010) up to level 2 for the H and V polarizations. The HIPE-8-processed data are displayed in Fig. 1 and the pixel numbering (following the raster observation order) is also presented in this figure.

We extracted the 50 spectra (25 pixels, two polarizations) independently. Because we performed no absolute calibration, we analyzed the lines in terms of line-to-continuum ratio (l/c), after correcting the data for the double sideband (DSB) response of the instrument and assuming a sideband ratio of 0.5 (Roelfsema et al. 2012). Each pixel was treated for baseline-ripple removal when necessary by using a Lomb (1976) algorithm. Then, we checked if the observations had suffered any pointing offset. While the relative pointing uncertainty within the map should be very low, the position of the whole map with respect to Jupiter's center is subject to the pointing uncertainty of *Herschel*. The reason why we had to determine the true pointing for the map was to avoid confusing thermal/abundance variability effects with purely geometrical effects on the l/c. For instance, the effect of a pointing offset in a given direction leads to an increase/decrease of the line peak intensity in connection with limb-brightening in the line and limb-darkening in the continuum compared to what is obtained with the desired pointing. Retrieving the true pointing offset can be achieved by measuring the relative continuum level in the 50 spectra and comparing it to model predictions. For each polarization we measured the continuum in each pixel of the map and adjusted the pointing offset to minimize the residuals between the observations and the model in the 25 pixels. According to Roelfsema et al. (2012), the H and V receivers are misaligned by less than $1''$. We found that the continuum patterns seen in H and V could be reproduced with mean pointing offsets of ($-0\farcs7$, $-0\farcs7$) in right ascension and declination with differences between H and V of $\sim 0\farcs3$. The difference is small enough compared to the beam size that we averaged the H and V maps to improve on the noise.

Finally, we smoothed the 25 remaining spectra to a 12 MHz resolution to increase the S/N. As a result, the water line is detected in each pixel. The S/N we observe has a lowest value of 3.5 in pixels 1 and 21, generally ranges between 20 and 30, and reaches a maximum of 60 in pixel 17 (per 12 MHz channel).

2.1.2. *Herschel*/PACS maps

We first observed the full-range spectrum of Jupiter with the PACS spectrometer. This part of the instrument consists of an array of 5×5 detectors that covers $50'' \times 50''$ on the sky. The extreme far-infrared flux of Jupiter does not allow one to observe it with PACS in any standard mode. To avoid detector saturation, the spectrometer readout electronics were configured to the shortest possible reset intervals of 1/32 s. These observations (Observation ID: 1342187848) were carried out with the PACS spectrometer on December 8, 2009 (OD 208). Although these data, which cover the $\sim$50–200 μm range, will be published extensively in another paper (Sagawa et al., in prep.), we present

Table 1. Summary of *Herschel* observations of water in Jupiter.

OD	Obs. ID	UT start date	Int. time [s]	Freq. or Wav.	Instrument	Map properties	Beam size [″]	Size of Jupiter[a] [″ × ″]
208	1342187848	2009-12-08 13:07:58	23 538	58.7 μm & 65.2 μm	PACS	full range scan 2 × 2 raster & 28″ steps 100 points	9.4	36.94 × 34.54
419	1342200757	2010-07-07 08:16:36	2255	1669.904 GHz	HIFI	5 × 5 raster & 10″ steps 25 points	12.7	42.35 × 39.60
580	1342211204	2010-12-15 10:21:20	3001	66.4 μm	PACS	line scan 4 × 4 raster & 6.″5 steps 400 points	9.4	40.85 × 38.20

Notes. [(a)] Equatorial × Polar apparent diameter.

here two maps of the water emission at 58.7 μm and 65.2 μm, both extracted from the full-range spectrum. PACS has a spatial pixel (spaxel, hereafter) size of 9.″4 at these wavelengths. More details of these observations are given in Table 1. The line peak intensity ($l/c-1$, in % of the continuum) maps presented in Fig. 2 suggest that the water lines were a factor of 2 fainter in the north polar region than in the other limb regions. We took that as a possible clue for the horizontal distribution of water.

However, these observations were not optimized for mapping Jupiter's disk and will not be analyzed quantitatively below. Indeed, the observation consisted of a 2 × 2 raster with a stepsize of 28″ to have the disk seen once by every spaxel. Consequently, the planetary disk contains only a few pixels. These observations were also full grating scans with much time between the up-scan and the down-scan for a given line, which implies larger systematics in the data. The dominant source for the "noise" may be the spacecraft pointing jitter, which mainly affects spaxels that see parts of the limb or are close to the limb, because even small jitter can cause significant flux variations within a spaxel. Moreover, the observed line width varies from one pixel to another in the PACS maps. The key for the variation is the source position and source extension within the spectrometer slit. A point source will by default have a narrower profile than an extended source. For an extended source, even if 25 spatial spectra are taken at the same time, the profiles will depend on how each of the spaxels is filled by the source. In this way, there are certainly limb effects when observing planets like Jupiter and Saturn. For instance, there is up to a factor of 2 difference between the highest and lowest line width in the 58.7 μm map. Indeed, the mean values and standard deviations of the observed line widths are 0.0153 μm and 0.0041 μm at 58.7 μm and 0.0100 μm and 0.0022 μm at 65.2 μm. Such high values for the standard deviations with regard to the mean values prevent any meaningful quantitative analysis and interpretation of these maps. However, these rough mapping observations definitely encouraged us to perform a deeper integration with a dedicated and optimized mapping observation of a stronger water line.

We obtained a water map at 66.4377 μm (=4512 GHz) with PACS (Observation ID: 1342211204) on December 15, 2010 (OD 580). The spaxel size was also 9.″4 at this wavelength. To cover the entire disk of Jupiter and slightly beyond in the best way, we defined a 4 × 4 raster with a stepsize of 6.″5. At each raster position a single grating up/down scan around the 66.4377 μm water line was executed in unchopped mode to avoid transient effects at this extreme flux range. The duration of the entire raster including overheads was 3001 s (more details in Table 1). Given the PACS beam FWHM of 9.″4 at 66.4 μm and the enormous signal, the water line could be measured at all raster positions, even to about 10″ beyond the limb.

The response of the PACS Ge:Ga detectors increases with the strength of the cosmic radiation field, but at the same time it decreases because of the strong infrared illumination. Therefore the response is continuously drifting throughout the entire Jupiter measurement and an absolute flux calibration of the spectra cannot be achieved within any reasonable uncertainty. However, when expressing the line spectra in terms of l/c, the uncertainty in the absolute response cancels out and opens the path to a relevant analysis.

The data reduction started from the Level 0 products that were generated according to the descriptions in Poglitsch et al. (2010). Level 1 processing was run within HIPE 8.0 through all standard steps for unchopped observations. All additional processing (flat-fielding, outlier removal and rebinning) was carried out with standard IDL tools.

The astrometric coordinates of Jupiter, taken from the JPL Horizons database, were subtracted from the product coordinates after interpolating them to the respective sample times. For each spectrum and spaxel of the integral field spectrometer, a single averaged relative (with respect to Jupiter's center) coordinate was computed and used for the spectral image reconstruction. As in the HIFI map reduction, we retrieved the true pointing. The observed line width values are much more uniform over the entire map: its mean value and standard deviation is 0.0105 μm and 0.0010 μm. To exclude these small variations, we adapted the spectral resolution in our radiative transfer computations to the value measured in each pixel.

Using all spaxels at the 16 raster positions, a total of 400 spectra were recorded with a resolving power ($R = \lambda/\Delta\lambda$) of 6400 on average. The resulting map is presented in Fig. 3. The S/N in the map is generally ~30 but reaches values twice as high at some positions. The spectra were then divided by a third order polynomial fit to the continuum, excluding the range of the water line. Because the line profiles are purely instrumental at this resolving power, they were analyzed by fitting with a Gaussian line profile. Therefore, all abundance and temperature information is contained in the line peak + line width, i.e., in the line area, in the map.

Below, we analyze the PACS and HIFI data according to their l/c. Because the *Herschel* mapping observations of water are sensitive to the temperature and water abundance distributions, we have monitored the temperature over the Jovian disk

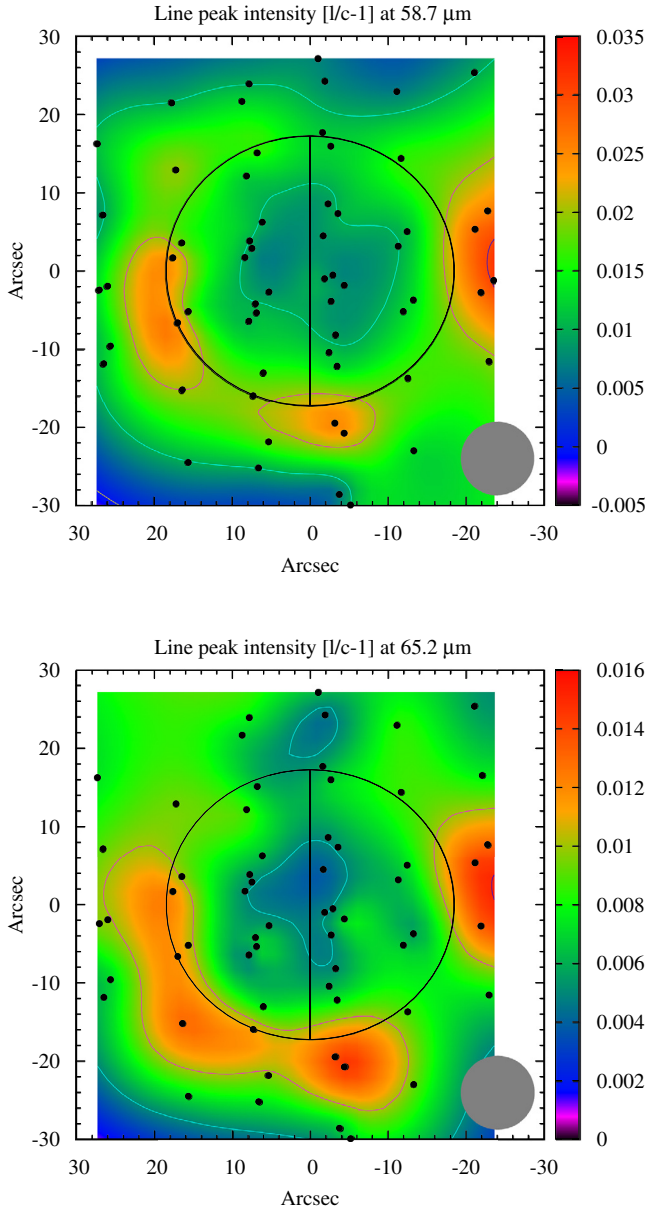

Fig. 2. Water maps of the line peak intensity (=l/c-1, thus in % of the continuum) at 58.7 and 65.2 μm observed by the PACS spectrometer on December 8, 2009. Jupiter is represented by the black ellipse, and its rotation axis is also displayed. The beam is represented by a gray filled circle. Both maps indicate that there is less emission in the northern hemisphere than in the southern (best seen in the limb emission).

and carried out complementary ground-based observations at the NASA Infrared Telescope Facility (IRTF) in 2009 and 2010.

2.2. IRTF observations

2.2.1. IRTF/TEXES maps

On May 31 and October 17, 2009, we performed observations with the Texas Echellon cross-dispersed Echelle Spectrograph (TEXES; Lacy et al. 2002), mounted on the NASA IRTF atop Mauna Kea. By achieving a spectral resolving power of ~80 000 in the ν_4 band of methane (CH_4) between 1244.8 and 1250.5 cm^{-1} (see Fig. 4), we were able to resolve the pressure-broadened methane emission wing features, which give detailed information on the vertical temperature profile from 0.01

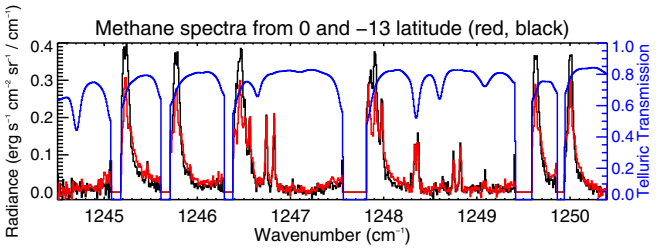

Fig. 4. Methane emission spectra from 13 °S latitude (black) and from the equator (red) showing the different spectral shape and strength from the May 2009 observations with TEXES. The spectra are at an airmass between 1 and 1.2. The blue curve represents the telluric transmission. Owing to the high Jupiter/Earth velocity and the high spectral resolution achieved by TEXES, we were able to easily separate the Jovian methane emission from the telluric methane absorption. Gaps in the data are caused by telluric transmission regions that are too opaque to retrieve useful data. The red and black spectra have been flat-fielded by the black chopper wheel minus the sky emission, which performs a first-order division of the atmosphere.

to 30 mbar. The data were reduced through the TEXES pipeline reduction software package (Lacy et al. 2002), where they were sky-subtracted, wavelength-calibrated, and flux-calibrated by comparing them to observations of a black chopper wheel made at the beginning of each set of four scan observations. We subsequently processed the pipelined data through a purpose built remapping software program to co-add all scan observations and solve for the latitude[1] and west longitude of each mapped step and spaxel along the TEXES slit length. The data were then zonally averaged and binned into latitude and airmass bin sizes of 1−1.2, 1.2−1.5, 1.5−2.0, and 2.0−3.0 Jovian airmass. The latitude bins (Nyquist-sampled spatial resolution) varied from 2 degrees at the sub-Earth point to 5 degrees at −60 degrees latitude.

2.2.2. IRTF/MIRSI maps

In addition to the TEXES observations, we recorded two sets of radiometric images of Jupiter's stratospheric thermal emission observed through a discrete filter with a FWHM of 0.8 μm, centered at a wavelength of 7.8 μm with the Mid-Infrared Spectrometer and Imager (MIRSI; Kassis et al. 2008) that is also mounted on the NASA IRTF. The radiance at this wavelength is entirely controlled by thermal emission from the ν_4 vibrational-rotational fundamental of methane and emerges from a broad pressure region in the middle of Jupiter's stratosphere, 1−40 mbar (see Fig. 2 of Orton et al. 1991). Because methane is well-mixed in Jupiter's atmosphere, any changes of emission are the result of changes in temperature around this region of Jupiter's stratosphere. The images were made (i) on 25 June−1 July 2010, very close in time to the July 7 HIFI observations, and (ii) on 5−6 December 2010, very close in time to the December 15 PACS observations. An example of these observations is shown in Fig. 5.

The data were reduced with the standard approach outlined by Fletcher et al. (2009), in which they were sky-subtracted with both short- (chop) and long-frequency (nod) reference images on the sky. The final results were co-additions of five individual images with the telescope pointing dithered around the field of view to fill in bad pixels in the array and minimize the effects of non-uniform sensitivities of pixels across the array. Before coadding, the individual images were flat-fielded using a

[1] All latitudes in this paper are planetocentric latitudes.

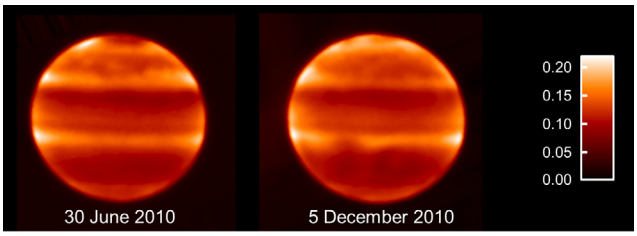

Fig. 5. IRTF/MIRSI radiance observations at 7.8 μm in the ν_4 rotational-vibrational band of methane in Jupiter. These radiance images, recorded on June 30 (*left*) and December 5 (*right*), 2010, are essentially sensitive to the stratospheric temperature between 1 and 40 mbar. The radiances are given in erg/s/cm^2/cm^{-1}/ster.

reference to observations of a uniform heat source, a part of the telescope dome. The images were also calibrated for absolute radiance by convolving the filter function with spectra taken by the Voyager IRIS and Cassini CIRS experiments, also described in detail by Fletcher et al. (2009).

3. Modeling

3.1. Herschel data modeling

We analyzed the *Herschel* maps with a 1D radiative transfer model that was improved from the model presented in Cavalié et al. (2008a). Our code is written in ellipsoidal geometry and accounts for the limb emission and the sub-observer point position. We included the opacity caused by the H_2-He-CH_4 collision-induced absorption spectrum (Borysow et al. 1985, 1988; Borysow & Frommhold 1986) and by the far wings of ammonia (NH_3) and phosphine (PH_3) lines. We used the JPL Molecular Spectroscopy catalog (Pickett et al. 1998) as well as H_2/He pressure-broadening parameters parameters for water lines from Dutta et al. (1993) and Brown & Plymate (1996).

As baseline, we used the same temperature profile as in Cavalié et al. (2008b) and Cavalié et al. (2012), which was taken from Fouchet et al. (2000) (see Fig. 6). The PACS observations probe pressures lower than 2 mbar (see Fig. 7). In this way, we constructed a series of thermal profiles, based on our nominal profile, with 1-K-step temperature deviations at pressures lower than 2 mbar to determine the necessary temperature deviations from our nominal profile to fit the observations. These deviations were then checked for consistency with our IRTF thermal maps. The deviations from our nominal thermal profile are initiated at 10 mbar to obtain a smooth transition toward the modified thermal profile compared to our nominal profile (and to avoid introducing a temperature inversion layer in the 1−10 mbar pressure range for negative deviations). For each thermal profile, we recomputed the pressure-altitude relationship assuming hydrostatic equilibrium. The resulting thermal profiles are shown in Fig. 6.

Retrieving the water vertical profile from the HIFI spectra will be the object of a forthcoming paper (Jarchow et al., in prep.) and therefore will not be addressed here. We used profiles that are qualitatively representative of the IDP and SL9 sources. For the IDP source, we took the profile published in Cavalié et al. (2008b), which corresponds to a water input flux of 3.6×10^6 cm^{-2} s^{-1}. This profile was obtained with a photochemical model that used the same thermal profile as our nominal profile and a standard $K(z)$ profile (Moses et al. 2005). This profile enables one to reproduce the average line intensity on the HIFI map. For the SL9 source, we took an empirical profile in

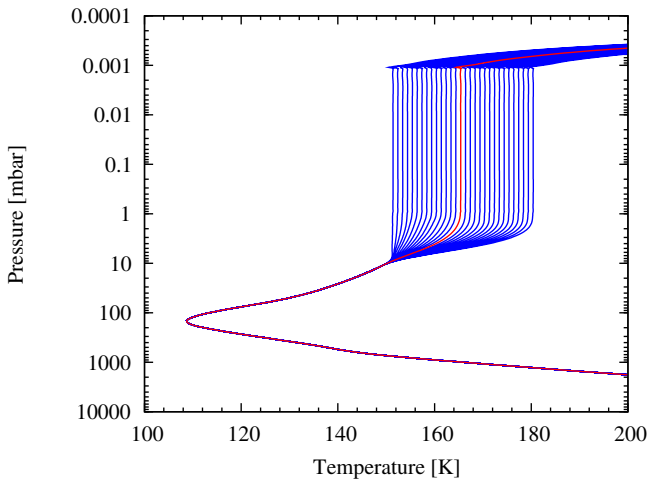

Fig. 6. Examples of temperature profiles used in this study. Our nominal profile is displayed in red. The thermal profiles displayed in blue correspond to cases in which the temperature at pressures lower than 2 mbar is increased or decreased with 1-K steps from −14 to +15 K. The deviations from our nominal thermal profile are initiated at 10 mbar to smooth the transition from the nominal profile at higher pressures toward the modified thermal profile at lower pressures.

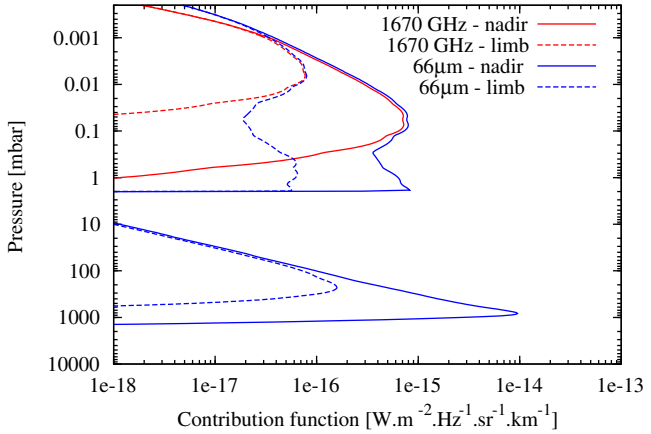

Fig. 7. Contribution functions of the water lines at 1669.9 GHz and 66.4 μm at their respective observed spectral resolutions for a pencil-beam geometry. These profiles have been obtained with the water profile used in this work (all water constrained to pressures lower than 2 mbar).

which water is restricted to pressures lower than a given pressure level p_0 (to be determined by our analysis). Both profiles are shown in Fig. 8.

The effect of the rapid rotation of the planet, which can clearly be seen as red or blue Doppler shifts of the water lines on the HIFI spectra (see Fig. 1) was taken into account, as well as the spatial convolution due to the beams of the HIFI and PACS instruments. Although the model assumes homogeneous temperature and water abundance within a HIFI or PACS beam, the geometry was fully treated. Indeed, the entire Jupiter disk was divided into small elements, including the limb. We solved the radiative transfer equation at each point and accounted for the Doppler shifts caused by the rapid rotation of Jupiter before finally performing the spatial convolution by the instrument beam.

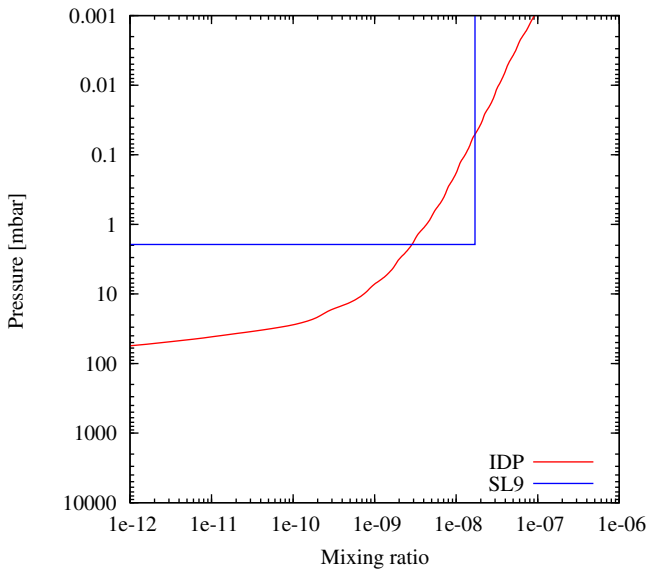

Fig. 8. Nominal water vertical profiles used in the analysis of the HIFI and PACS maps. The IDP profile (red solid line) was computed with the photochemical model of Cavalié et al. (2008b), using the nominal thermal profile of Fig. 6 and a standard $K(z)$ profile from Moses et al. (2005). In the SL9 profile, a cut-off level was set to $p_0 = 2$ mbar. This is the highest value of p_0 that enables reproducing all the HIFI lines. In this profile, the water mixing ratio is 1.7×10^{-8} as in the central pixel (number 13) of the HIFI map.

3.2. IRTF data modeling

Methane emission can be used to probe Jupiter's stratospheric temperatures because (i) the ν_4 band of methane emits on the Wien side of Jupiter's blackbody curve; (ii) methane is well-mixed throughout Jupiter's atmosphere and only decreases off at high altitudes because of diffusive separation (Moses et al. 2000); (iii) the deep volume mixing ratio is known from the Galileo probe re-analysis results of Wong et al. (2004) to be equal to $2.37 \pm 0.57 \times 10^{-3}$, resulting in a mole fraction of $2.05 \pm 0.49 \times 10^{-3}$. For the TEXES data, we used the photochemical model methane mole fraction profile from Moses et al. (2000) with a deep value of 1.81×10^{-3} taken from the initial Galileo probe results paper by Niemann et al. (1998) because it agrees within errors with Wong et al. (2004). Moreover, the Moses et al. (2000) model has been shown to agree with previous observations of Jupiter.

To infer Jupiter's stratospheric temperatures from the TEXES maps, we employed the automated line-by-line radiative transfer model described in Greathouse et al. (2011). This model uses the pressure-induced collisional opacity of H_2-H_2, H_2-He, and H_2-CH_4 as described by Borysow et al. (1985, 1988) and Borysow & Frommhold (1986) and the molecular line opacity for $^{12}CH_4$, $^{13}CH_4$, and CH_3D from HITRAN (Rothman et al. 1998). It also varies the vertical temperature profile to reproduce the observed methane emission spectra. The resulting zonally averaged temperature maps are displayed in Fig. 9. The pressure range we are sensitive to with these observations is 0.01−30 mbar.

A second approach to deriving stratospheric temperatures, which we applied to our MIRSI maps, consists of using the radiometrically calibrated versions of the 7.8 μm images. Although these maps yield only temperatures at a single level (between 1 and 40 mbar), they can differentiate between the thermal models shown in Fig. 6. Therefore, we simulated the 7.8 μm radiance we would expect from the range of temperature profiles from Fig. 6 to create a table of radiance vs. emission angle. Then we determined the upper-stratospheric temperature corresponding to the profile that most closely produced the observed radiance at each latitude/emission angle pair along the central meridian for each date. Orton et al. (1991) used a similar approach in their analysis of raster-scanned maps of Jupiter. The result is the temperature maps that are shown in Fig. 10. The zonal variability is much smaller than the meridional variability in each image, validating the approach taken in examining the zonal-averaged temperatures from the TEXES data shown in Fig. 9.

The *Herschel* observations are sensitive to pressures lower than 2 mbar. This is why we created the range of thermal profiles shown in Fig. 6, in which the profiles start to differ from one another at pressures lower than 10 mbar. This introduces the main limitation in our temperature derivation from the MIRSI images, because these observations are sensitive to levels ranging from 1 to 40 mbar. To encompass the range of observed radiances that are generated by higher temperatures in the 1−40 mbar range, we therefore had to increase the range over which we were perturbing the temperatures at pressures lower than 10 mbar. As a result, the temperatures derived from the MIRSI images are excessively high at latitudes corresponding to bright bands. Therefore, only the trend in the latitudinal variation of the temperature can be relied on rather than the values themselves.

4. Results

4.1. HIFI map

At 1669.9 GHz and with the spectral resolution of HIFI, we probed altitudes up to the 0.01 mbar pressure level, depending on the observation geometry (see Fig. 7). The line opacity at the central frequency at the observed spectral resolution but at infinite spatial resolution is ∼10 at the nadir and ∼250 at the limb. We first tested the IDP profile (presented in the previous section) that fitted the SWAS and Odin observations in Cavalié et al. (2008b, 2012). At Jupiter, this source should be steady and spatially uniform (Selsis et al. 2004). In the case of a steady local source, it would either show high concentrations at high latitudes (for material transported in ionic form) or at low latitudes (for material transported in neutral form). We detected neither of these cases in the observations, although this diagnostic is limited by the relatively low spatial resolution. The result of the IDP model is displayed in Fig. 11. The IDP profile fails to reproduce the observations in several aspects. Indeed, it can be seen that this model produces lines that are too strong in most of the northern hemisphere (pixels 6, 7, 15 and 16). Figure 12 shows that if the water flux attributed to IDP is lowered to $\sim 2.0 \times 10^6$ cm^{-2} s^{-1}, the model matches the observations in terms of l/c but still overestimates the line width. The main problem of this model is that the line wings are too broad in most of the pixels. The only pixels in which the line wings could be compatible with the data are pixels with the highest noise. This means that the bulk of the stratospheric water is not located just above the condensation level, i.e., at ∼20−30 mbar as in the IDP model, but higher in altitude. The line shape of the 556.9 GHz water line as observed by SWAS and Odin already suggested that the IDP source was unlikely (Cavalié et al. 2008b). Consequently, the IDP model can be ruled out. In contrast, the SL9 profile gives much better results in the line wings (see Fig. 11). We found that all line wings could be reproduced

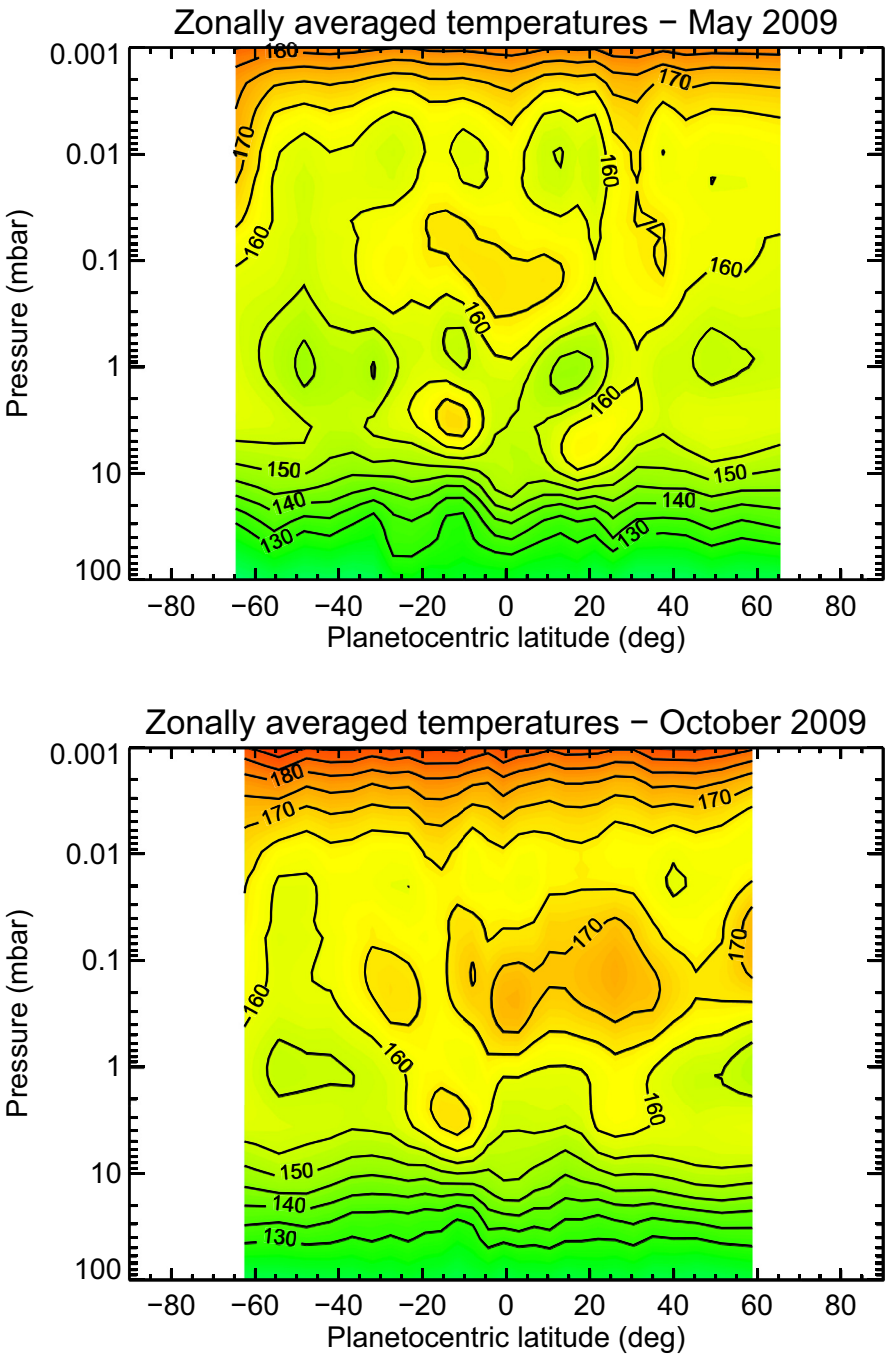

Fig. 9. Zonally averaged thermal maps as retrieved from IRTF/TEXES observations of the ν_4 band of methane carried out on May 31 and October 17, 2009. The sensitivity ranges from 0.01 to 30 mbar.

provided that the p_0 level was not set at pressures higher than 2 mbar[2]. For the remainder of the paper, we have set the p_0 level to this value.

Before we more quantitatively analyze the SL9 model results with regard to the HIFI observations, we focus on the PACS map analysis using the information on the p_0 level we derived above. Because we already ruled out the IDP model at this stage, we do not use it further in the analysis.

[2] The value of p_0 can be set to pressures lower than 2 mbar and still reproduce the observations reasonably well, provided that additional water was included in the model. Indeed, Doppler broadening is about equal to pressure broadening around the 1 mbar level in Jupiter's atmosphere. Therefore, the line widths will be almost the same in models with a value of p_0 lower than 2 mbar.

4.2. PACS maps

We now use the PACS maps to separate the temperature and water vapor variability. First, we can see that the line peak intensity ($=I/c - 1$) maps (Figs. 2 and 3) present the same spatial structure. The highest emission is concentrated at the limb due to limb-brightening in the line and limb-darkening in the continuum. The main feature seen in these maps is the lack of emission around the northernmost region compared to the southernmost region. However, we have to keep in mind that because the observations are not spectrally resolved, all information on the temperature and water column abundance is contained in the line area. The line peak intensity alone only contains part of the information. Therefore, we fitted the line peak with an adjustable line width in the model, which is the same as fitting the line area. The line opacity at the central frequency at the observed spectral

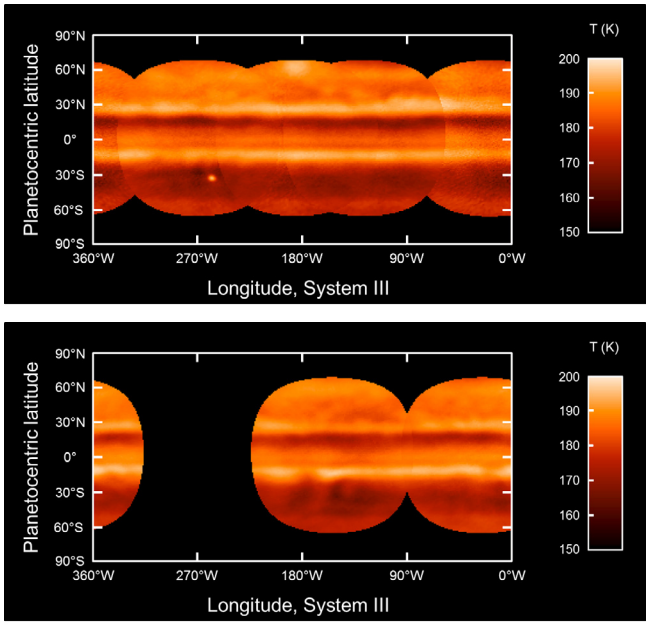

Fig. 10. IRTF/MIRSI radiance observations at 7.8 μm in the ν_4 rotational-vibrational band of methane, carried out on 25 June–1 July 2010 (*top*) and 5–6 December 2010 (*bottom*). These observations are essentially sensitive to the stratospheric temperature between 1 and 40 mbar. The color scale gives the correspondence between radiances and stratospheric temperatures at 2 mbar, according to our derivation procedure (see text for limitations). These maps suggest that the northern hemisphere is generally warmer than the southern hemisphere. The bright belt seen around 15 °S in both maps (as well as in the TEXES data; see Fig. 9) is a possible explanation for the ~4 K increase seen in the PACS 66.4 μm map between the equator and 25 °S. The bright dot seen in the 25 June–1 July 2010 map is Io and had only marginal effects on the zonal mean results.

resolution but at infinite spatial resolution is ~3 at the nadir and ~100 at the limb.

To investigate whether this north-south asymmetry is caused by the stratospheric temperature distribution or by the column density spatial distribution, we analyzed the 66.4 μm emission map considering two cases:

- We determined the spatial distribution of the temperature deviation from the nominal profile at pressures lower than 2 mbar from our nominal thermal profile considering a spatially uniform distribution of water. In this case, we set the water mixing ratio to 2×10^{-8} for $p \leq 2$ mbar, corresponding to a column abundance of 3.7×10^{15} cm^{-2}. This choice roughly corresponds to the average column found in this map. Its choice is thus arbitrary to some extent but does not affect the result, because we are interested in relative contrasts in temperature over Jupiter's disk, not in absolute values of them.
- We determined the spatial distribution of the column density considering a spatially uniform temperature profile (i.e., our nominal profile).

4.2.1. Map of the stratospheric temperature deviation from the nominal profile

We used the thermal profiles shown in Fig. 6 to check whether latitudinal temperature variations could cause the line peak emission distribution observed in Fig. 3, assuming a spatially uniform distribution of water. To do this, we fitted the line in each pixel of the map by finding the most appropriate thermal profile and retained the temperature deviation from the nominal profile associated to each pixel. The temperature deviation map associated to the 66.4 μm observations is shown in Fig. 13. The uncertainty on the line peak values is in the range of 3–10%, which translates into an uncertainty of 1–3 K on the derived temperature deviation. Another way to evaluate the uncertainty on the temperature is to see the variations of the temperature around a given latitude. Although the atmosphere radiative timescale is 3 orders of magnitude longer than the rotation period (Flasar 1989), variations of several K in the zonal temperatures at 1 mbar, probably caused by a Rossby wave trapped at certain latitudes, have been reported by Flasar et al. (2004). However, at our spatial resolution, the temperature should be smoothed in longitude compared to Flasar et al.'s observations. After checking the temperatures in several narrow latitudinal bands, we found a scatter of ~3 K on the temperature, which agrees with the uncertainty range we derived.

The 66.4 μm map in Fig. 13 shows two interesting structures that can also be better seen in a representation of the temperature deviation from the nominal profile as a function of latitude. Such a latitudinal section is shown in Fig. 14.

First, a north-south contrast of 10–15 K (with higher temperatures in the southern hemisphere) is required to reproduce the global north-south asymmetry seen in the line peak emission. This picture contradicts the TEXES maps from 2009 (see Fig. 9). In these maps, we see large meridional variations at 2 mbar (see Fig. 14), of the same order of magnitude as in our PACS map (~10 K). These variations correlate quite well with those seen by Fletcher et al. (2011) at 5 mbar in 2009–2010. But there is no evidence for a global meridional asymmetry. Moreover, there clearly are changes in the stratospheric temperature field between 2009 and 2010, as shown by the thermal maps we retrieved from the 7.8 μm IRTF/MIRSI images we captured a few days before the HIFI and PACS maps were produced (see in Fig. 10). However, these changes do not work in favor of the temperature variability hypothesis to explain the water emission maps. On the contrary, the Jovian quasiquadriennial oscillation (Leovy et al. 1991) creates a bright band north of the equator that we only marginally see in Fig. 13. Accordingly, the MIRSI observations even suggest that there the temperatures are higher in the northern hemisphere than in the southern hemisphere in the pressure range we are sensitive to. The opposite would have been necessary to explain the water emission maps. Consequently, the asymmetry we see in the water emission maps has to be due to an hemispherical asymmetry in the water distribution.

The second structure we see in the 66.4 μm map is a temperature increase of ~4 K between 25 °S and the equator. There is a good correlation between this feature and a warm temperature belt seen consistently between 1 and 30 mbar in the MIRSI and TEXES data and in Fletcher et al. (2011) around 15 °S. This feature likely results from the spatial convolving of this warm belt (see Fig. 14). We discuss it in Sect. 5.1.

Now that we have proven that a global latitudinal temperature variation is not the cause for the north-south asymmetry seen in the line peak intensity maps, we can derive the column density map that reproduces the observations.

4.2.2. Column density map

Here, we assumed that our nominal temperature profile is valid at any latitude/longitude and locally rescaled the water vertical profile, i.e., the water column density, to fit the line in each pixel. The computed column densities are representative of averages

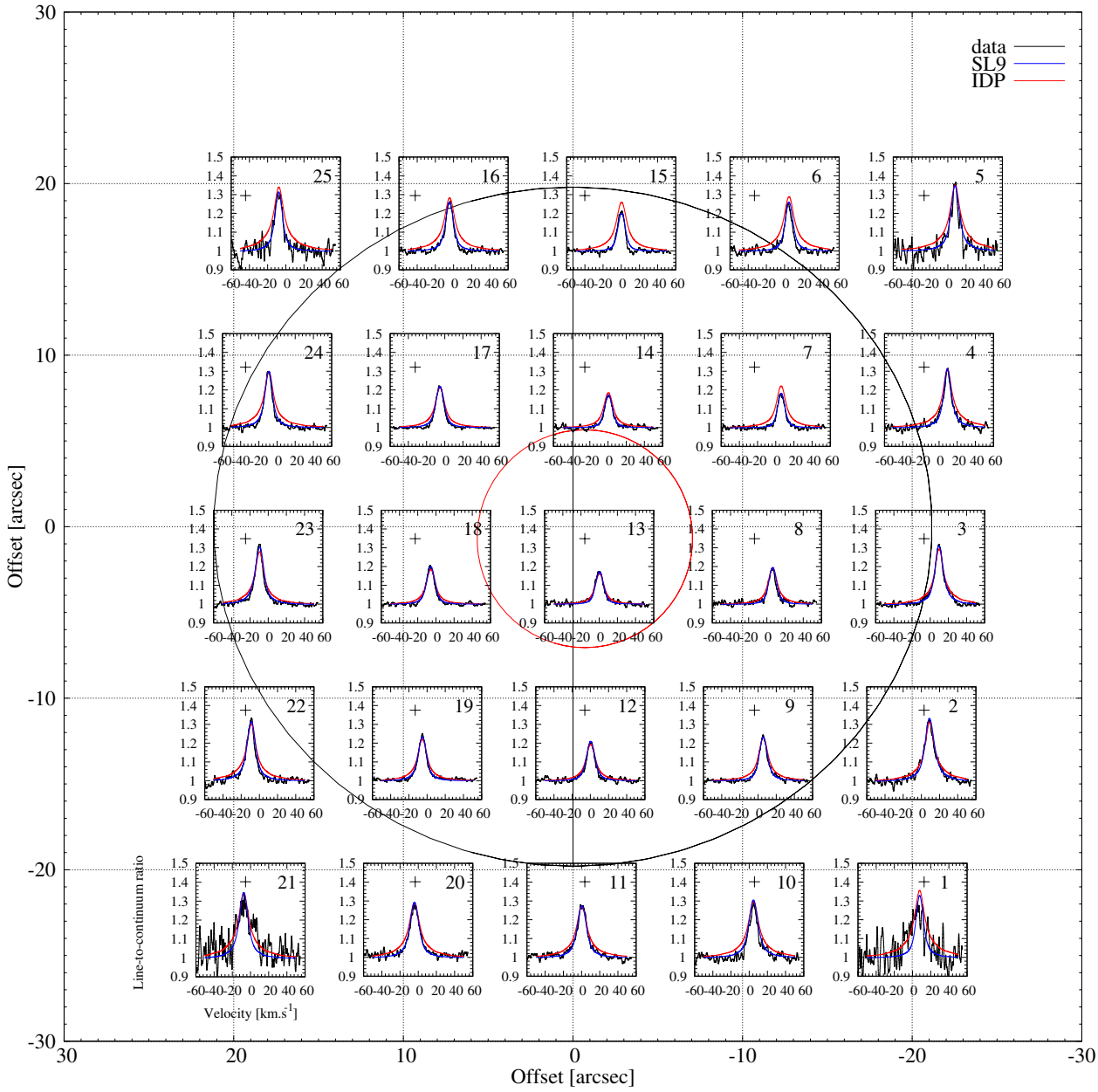

Fig. 11. Water 5 × 5 raster map at 1669.9 GHz obtained with *Herschel*/HIFI on July 7, 2010, expressed in terms of l/c and smoothed to a spectral resolution of 12 MHz (observation are plotted in black). Jupiter is represented with the red ellipse, and its rotation axis is also displayed. The black crosses indicate the center of the various pixels after averaging the H and V polarizations. The beam is represented for the central pixel by the red dotted circle.These high S/N observations rule out the IDP source model (red lines) because they result (i) in narrower lines than the ones produced by the IDP model; and (ii) in a non-uniform spatial distribution of water. Even if the flux in the northernmost pixels is adjusted to lower values to fit the l/c, the IDP model fails to reproduce the line wings (see Fig. 12). By adjusting the local water column density by rescaling the SL9 vertical profile, we find that an SL9 model (blue line), in which all water resides at pressures lower than 2 mbar, enables one to reproduce the observed map.

over the PACS beam. The resulting maps are displayed in Fig. 15 and a latitudinal section taken from the 66.4 μm map is shown in Fig. 16. The uncertainty on the line peak values translates into an uncertainty of up to 20% on the column density values. This is consistent with the scatter we find in narrow latitudinal bands (∼15%). If we had used a physical profile for the SL9-material evolution instead of an empirical one for water, we could have ended up with column density values different by a factor of up to 2 (with the same level of uncertainties). One needs to know the true vertical profile to retrieve the true values of the local water column.

The 66.4 μm map and the corresponding latitudinal section show a general trend in the latitudinal distribution of the derived column densities. Indeed, we see an increase by a factor of 2−3 from the northernmost latitudes to the southern latitudes. This kind of distribution was anticipated by Lellouch et al. (2002), though with a much lower contrast, from their SL9 model. They expected a contrast of only 10% between 60 °S and 60 °N at infinite spatial resolution in 2007. Here, we observe a factor of 2−3 contrast between 60°S and 60 °N after spatial convolution by the instrument beam. This should translate into an even stronger contrast at infinite spatial resolution.

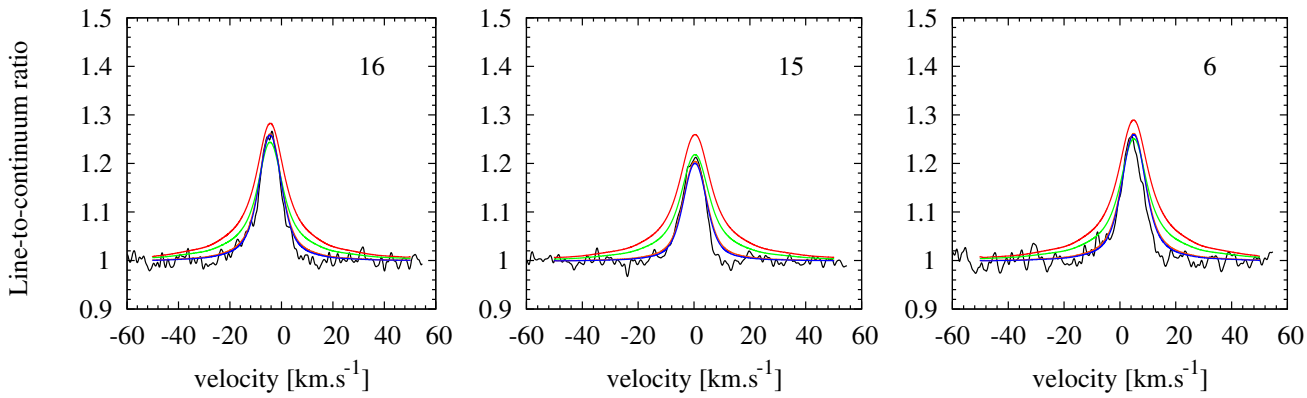

Fig. 12. Zoom on the northernmost pixels 6, 15 and 16 of the HIFI map. The SL9 model is displayed in blue, while the IDP model with a flux of 3.6×10^6 cm^{-2} s^{-1} is plotted in red. The IDP model overestimates both the l/c and the line width in each pixel. Even if the IDP flux is lowered to 2.0×10^6 cm^{-2} s^{-1} (green line) to roughly fit the l/c, it still fails to fit the wings. A model based on the philosophy of the "hybrid" model of Lellouch et al. (2002) with the SL9 source and a background IDP source with a flux of 8×10^4 cm^{-2} s^{-1}, corresponding to the upper limit placed on the IDP source by the authors, is shown in orange. This model can barely be distinguished from the pure SL9 model, which means that an IDP background source is compatible with our observations.

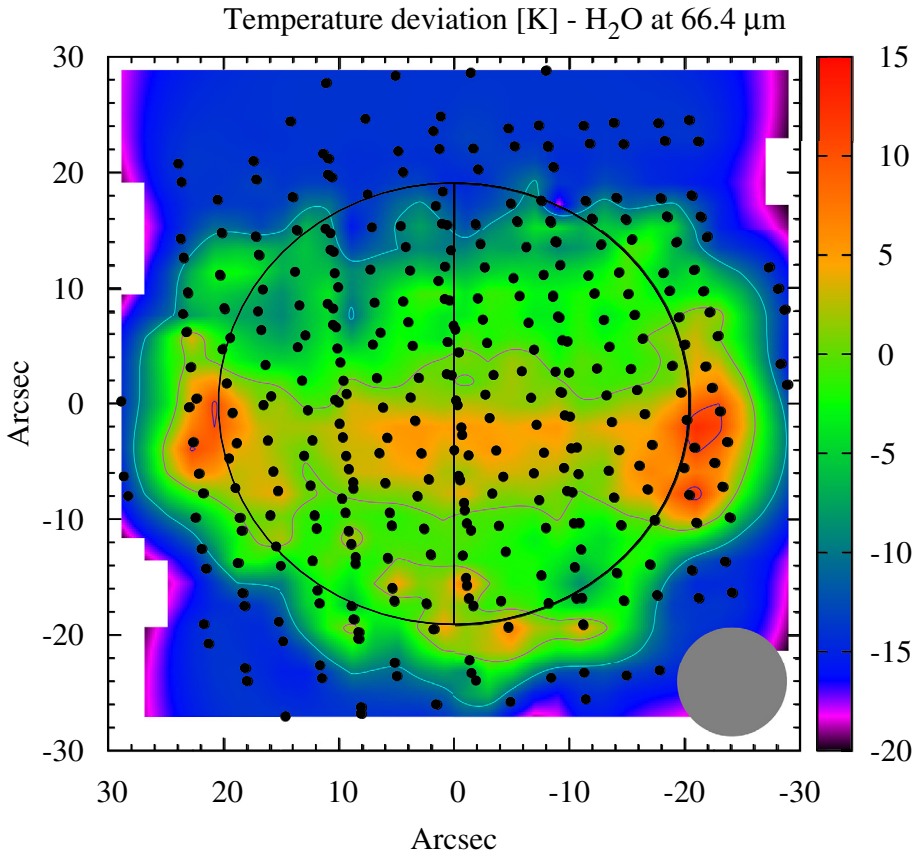

Fig. 13. Map of the temperature deviation (in K) from the nominal thermal profile assuming a spatially uniform distribution of water, as derived from the 66.4 μm map. Jupiter is represented by the black ellipse, and its rotation axis is also displayed. The beam is represented by the gray filled circle. A relative difference of 10−15 K in the high stratospheric temperatures between the northern and southern latitudes is required to reproduce the observations. A warm south equatorial region (0−25 °S) of ∼4 K higher stratospheric temperatures is identified in this map (see also Fig. 14).

We applied the same methodology as for the PACS map to derive the local column density from the HIFI map, still assuming a spatially uniform temperature. The resulting map is shown in Fig. 17. The uncertainty on the column abundance derivation is on the order of 20% in the HIFI pixels despite the high S/N, because the line is optically thick. We find that the column abundance increases from the northernmost latitude to the southern latitudes by a factor of ∼3. The general trend as a function of latitude as well as the highest values of the water column ($4-5 \times 10^{15}$ cm^{-2}) fully agree with the PACS results obtained at 66.4 μm and therefore confirm our results.

5. Discussion

5.1. A local temperature maximum or an additional source of water around 15 °S?

In the 66.4 μm map analysis (Sect. 4.2.1), we found that the emission between the equator and 25 °S could be explained by either an about 4 K warmer stratospheric temperature and/or a higher water column density (or even a combination of both), over the PACS beam.

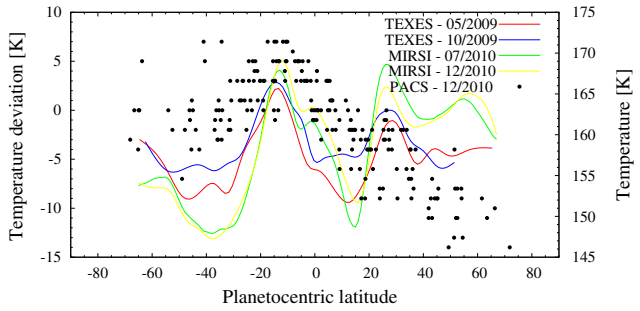

Fig. 14. Latitudinal section of the temperature deviation from the nominal profile as derived from the 66.4 μm map (black points), assuming a spatially uniform distribution of water. Only the pixels within the planetary disk are represented here. The temperatures at a pressure of 2 mbar as retrieved from our IRTF/TEXES observations are also displayed (red line for the May 2009 data and blue line for the October 2009 data) as well as the temperatures derived from our IRTF/MIRSI data (green for July 2010 and yellow for December 2010). The temperatures derived from the MIRSI images are averages for the pressure range the observations are sensitive to (1−40 mbar). We applied to these values an offset of −20 K to bring them to the same scale as the TEXES values (see Sect. 3.2 for the reasons why we obtained these high values from the MIRSI data). The warm temperature belt seen around 15 °S is the most probable cause for the enhanced emission seen at these latitudes in our 66.4 μm map (see Fig. 13). There is only marginal evidence in the water emission observations for the warm belt seen in the IRTF/MIRSI data around 30 °N.

The IRTF/MIRSI images unveil a warm belt around 15 °S at pressures between 1 and 40 mbar (see Fig. 5), also seen in the data of Fletcher et al. (2011) at 5 mbar. The temperature maps retrieved from the IRTF/TEXES data locate such a belt at this latitude in the 1−10 mbar pressure range (see Fig. 9) and it is most obvious at 2 mbar (see Fig. 14). Given that the temperature excess needed over the PACS beam to fit the data is ∼4 K, this warm belt is probably sufficient to explain the enhanced water emission in this latitudinal range. This warm belt also implies that the water condensation level is located at a slightly lower altitude, allowing higher column densities of water at these latitudes.

On the other hand, if the warm belt is not sufficient and if the water column is indeed higher at these latitudes (independently of any temperature effect), this means that this extra water is provided by an additional source. What kind of source could that be? A local source (rings/satellites) that would generate these spatial properties seems unlikely. If the material were transported from the source to Jupiter in neutral form, the deposition latitude should be centered on the equator. According to Hartogh et al. (2011), this is how the Enceladus torus feeds Saturn's stratosphere in water. A second possibility is the deposition of ionized material (with a high charge-to-mass ratio) at latitudes that are magnetically connected to the source(s), as proposed by Connerney (1986). According to his work, a source depositing material at ∼10 °S would probably need to be located at 1.1 planetary radii, in the case of Saturn. Because Jupiter's magnetic field is 20 times stronger than Saturn's, this would imply that a hypothetical source depositing material around 15 °S would need to be even closer to the planet than 1.1 Jupiter radii, a zone where there is no such source. There is no reason why a source like the IDP would deposit material only around 15 °S. In addition to that, an increase by a factor of ∼2 of the water column due to a local source or an IDP source should result in broader line widths in the pixels centered on the equator in the HIFI map, an effect evidently absent from Fig. 11. Finally, another possible source is an additional comet impact. The only known events are two impacts that have been detected in Jupiter between the SL9 event and our 2010 PACS observation. The first one occurred on July 19, 2009, but at a planetocentric latitude of 55 °S (Sánchez-Lavega et al. 2010; Orton et al. 2011). Interestingly, the second observed impact occurred on June 3, 2010, at a planetocentric latitude of 14.°5 S (Hueso et al. 2010). According to Hueso et al. (2010), this impactor had a size of 8−13 m. According to Fig. 16, the excess of H_2O column in this latitude region is on the order of $\sim 10^{15}$ cm^{-2}. The latitudinal band extending from 25 °S to the equator has a surface area of 1.35×10^{20} cm^2. The excess of water then corresponds to 4×10^9 kg of water, i.e., ∼3500 times the mass of a 3 m impactor consisting of pure water. It is thus unlikely that this extra water (if any) located between 25 °S and the equator is due to an additional external source.

Finally, we recall that the highest emission seen between 25 °S and the equator can most probably be attributed to the temperature increase in this region as seen in the MIRSI and TEXES maps (Figs. 9, 10 and 14).

5.2. Spatial distribution of water in Jupiter

The HIFI and PACS maps contain horizontal information on the water distribution in Jupiter's stratosphere. Because HIFI resolves the line shapes of the water emission at 1669.9 GHz, the HIFI map also contains information on the vertical distribution of the species if they are located at pressures lower than 1 mbar.

As stated previously, the precise shape of the vertical water profile will be retrieved from the 556.9, 1097.4 and 1669.9 GHz water lines observed at very high S/N with HIFI in the framework of the HssO Key Program and shall therefore be discussed in detail in a future dedicated paper (Jarchow et al., in prep.). However, we tested profiles that are qualitatively compatible with the IDP and SL9 sources. The spectral line shapes observed with the HIFI very high resolution confirm that the bulk of water resides at lower pressure levels (i.e., at pressures lower than 2 mbar) than would be the case with a steady IDP source. This result agree well with the prediction of Moreno et al. (2003) for the p_0 level (1 mbar) for CO, hydrogen cyanide (HCN), and carbon monosulfide (CS) 20 years after the SL9 impacts. Cavalié et al. (2012) studied the temporal evolution of the disk-averaged water line at 556.9 GHz with the Odin space telescope for almost a decade. They developed two models that could fit the tentatively seen decrease in the line contrast. In a first model, they tentatively increased the vertical eddy diffusion $K(z)$ by a factor of 3 at 1 mbar to remove more water by condensation. The line profiles in the HIFI map now show that this hypothesis is not valid and that the bulk of water remains at higher levels ($p_0 \leq 2$ mbar) than in their model, where the bulk of water had spread quite uniformly as a function of pressure down to the condensation level (see their Fig. 10). This means that the decrease of the line-to-continuum ratio at 556.9 GHz that they have tentatively observed has to be explained by the removal of water at the mbar and submbar levels and not by condensation. In a second model, Cavalié et al. (2012) approximately incorporated dilution effects from horizontal diffusion and chemical losses due to conversion of OH radicals (photolytical product of H_2O) into CO_2 based on the predictions of Lellouch et al. (2002) for their previously published temporal evolution model (Cavalié et al. 2008b). The water vertical profile used in Cavalié et al. (2008b) was based on the philosophy of the "hybrid model" of Lellouch et al. (2002), which took into account a low IDP flux of 4×10^4 cm^{-2} s^{-1}. This second model of Cavalié et al. (2012) has several advantages in

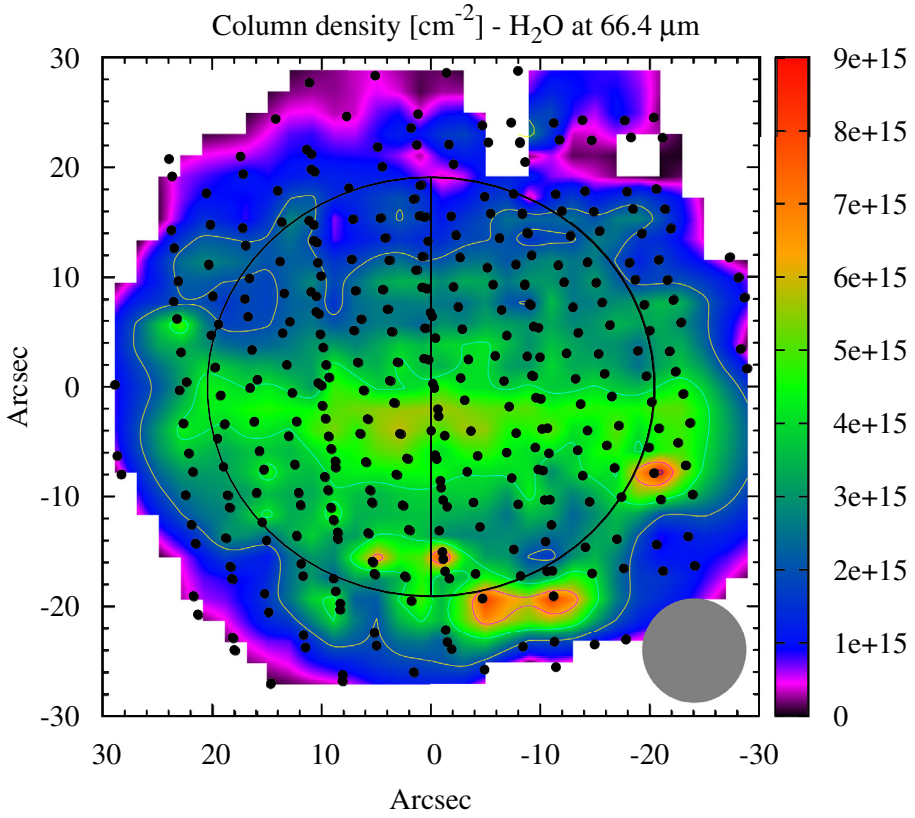

Fig. 15. Column density of water (in cm^{-2}), as derived from the 66.4 μm map. Jupiter is represented by the black ellipse, and its rotation axis is also displayed. The beam is represented by the gray filled circle. In the south equatorial region (0–25 °S), the emission maximum identified in this map is most probably caused by a temperature effect and not by a local maximum of the column density.

that enough water is lost as a function of time to reproduce the temporal evolution of the 556.9 GHz line, and it keeps a standard $K(z)$ profile and thus keeps the bulk of water at pressures compatible with our HIFI results. In this sense, it reconciles the Odin and our HIFI submillimeter observations of water with the infrared observations of ISO. Another advantage is that this model also accounts for a background IDP source with a flux of 4×10^4 $cm^{-2}\,s^{-1}$. According to our computations, adding an IDP source of that magnitude is not inconsistent with our observations, because such a low flux only marginally affects the line shape at 1669.9 GHz and 66.4 μm (e.g., Fig. 12). Even a model accounting for a background source due to IDP with a flux corresponding to the upper limit derived by Lellouch et al. (2002) (8×10^4 $cm^{-2}\,s^{-1}$) remains compatible with our data[3] (see Fig. 12). We are thus able to quantify how much of the observed water can be attributed to the SL9 impact. The disk-averaged column density of this SL9 + background IDP model (with a flux of 8×10^4 $cm^{-2}\,s^{-1}$) is $\sim 3 \times 10^{15}$ cm^{-2}, while the column density of the background IDP source alone is $\sim 10^{14}$ cm^{-2}. This means that more than 95% of the observed water comes from SL9 according to our models. These results are somewhat different from those obtained by Lellouch et al. (2002). These authors found a disk-averaged column of 1.5×10^{15} cm^{-2} from their SL9 + background IDP model and 4.5×10^{14} cm^{-2} for their background IDP model with a flux of 8×10^4 $cm^{-2}\,s^{-1}$, implying that up to 30% of the water could be due to IDP. These differences may arise from a different choice of chemical scheme, temperature, and vertical eddy mixing profiles. But both results essentially show that SL9 is by far the main source of water in Jupiter's stratosphere.

The HIFI and the 66.4 μm PACS maps consistently show a north-south asymmetry that cannot be attributed to a hemispheric asymmetry in the stratospheric temperatures but to an asymmetry in the water column abundance. If we omit the 25 °S-to-equator band from the meridional distribution observed by PACS shown in Fig. 16, which is most probably a result of a local temperature increase, we see that the water column looks roughly constant in the southern hemisphere and decreases linearly by a factor of 2–3 poleward in the northern hemisphere. This behavior is not expected from a IDP source but is consistent with the SL9 source, because the comet has hit the planet at 44 °S. Although the observations have taken place more than 15 years after the SL9 impacts, a remnant of the latitudinal asymmetry that was predicted by Lellouch et al. (2002) is now demonstrated, thus validating the SL9 source.

We have to keep in mind that, unlike Lellouch et al. (2006) for HCN and CO_2, we do not have access to latitudes higher than ~60° because of the observation geometry and beam convolution. It would thus be hazardous to directly compare of the water distribution with the distributions of HCN and CO_2 previously observed by Lellouch et al. (2006). They also correspond to different post-impact observation dates.

Lellouch et al. (2002) used a horizontal model that accounted for meridional eddy diffusion and a simplified chemical scheme for oxygen species to model the temporal evolution of the water column as a function of latitude. They derived a horizontal eddy diffusion coefficient of $K_h = 2 \times 10^{11}$ $cm^2\,s^{-1}$, constant in latitude, and a H_2O/CO ratio of 0.11 from their observed CO_2 horizontal distribution and disk-averaged water column. According to the results of this model, the contrast predicted for 2007 (i.e., even earlier than our *Herschel* maps) was ~10% at infinite spatial resolution. The contrast measured with PACS at 66.4 μm is

[3] This possible additional background source could also be attributed to a flow of smaller comets that would have impacted Jupiter at random latitudes in the last tens to a couple of hundreds of years, for which the vertical distribution of water would resemble that of a background IDP source.

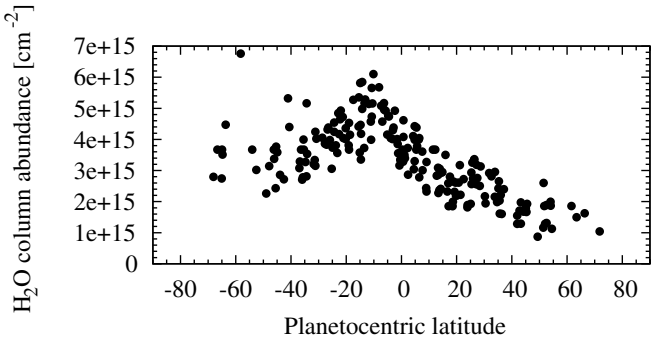

Fig. 16. Latitudinal section of the beam-convolved column density of water as derived from the 66.4 μm map. Only the pixels within the planetary disk are represented here. The peak values around 15 °S can most probably be attributed to the warmer temperatures observed around this latitude. The marginal increase seen around 30 °N could be due to the bright band detected at these latitudes in 2010 in the IRTF/MIRSI observations (see Fig. 14).

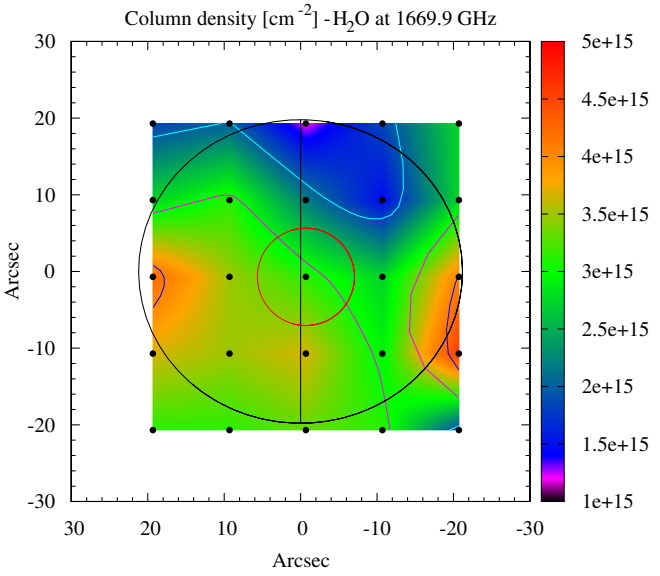

Fig. 17. Beam-convolved column density of water (cm^{-2}) map as derived from the HIFI observations at 1669.9 GHz. The beam is represented for the central pixel by the red circle.

already higher despite the beam convolution, which results in its attenuation. The deconvolution of the observed contrast to constrain horizontal transport is beyond the scope of this paper. However, we anticipate that if it were only due to eddy diffusion, the meridional distribution of water in Jupiter's stratosphere would require lower values for K_h. Lellouch et al. (2006) showed that the HCN meridional distribution in December 2000 (6.5 years after the impacts) could not be reproduced by using the latitudinally constant meridional eddy diffusion coefficient K_{yy} of Griffith et al. (2004). They rather had to invoke not only a K_{yy} variable in latitude (θ) with peak values of $K_{yy} \sim 2.5 \times 10^{11}$ $cm^2\,s^{-1}$, consistent with low spatial resolution measurements of Moreno et al. (2003), and a significant decrease of K_{yy} by an order of magnitude poleward of 40°, but also equatorward advective transport with wind velocities of ~7 $cm\,s^{-1}$. The equatorward advective wind results in a slower contamination of the northern hemisphere. According to this work and to Moreno et al. (2003), water and HCN are located at the same pressure level. If confirmed, they should be subject to the same horizontal transport regime. The philosophy of the transport model of Lellouch et al. (2006) seems to agree with our observations, but more modeling work is needed to check the consistency of their $K_{yy}(\theta)$ and wind velocity profiles.

We recall that the water column density values derived in this paper correspond to values convolved by the PACS beam. Because the 66.4 μm water line targeted for the mapping with PACS, from which the column densities were derived, is optically thick, there is no linear relation between the column densities and the observed lines. Therefore, it is not possible to simply spatially convolve the results of a diffusion model to compare it with our observation results. The confirmation of the validity of the horizontal model from Lellouch et al. (2006) with those data thus requires reproducing the observed map with a 2D (for geometry) radiative transfer model that could be fed with the water latitude-dependent distribution output of the diffusion+advection model. The problem is even more complicated because of the sensitivity of water to photolysis in Jupiter's high stratosphere and to condensation in the low stratosphere. Accordingly, unlike HCN and CO_2, water is not chemically stable and cannot be considered as an ideal tracer for horizontal dynamics. A 2D/3D photochemical model including oxygen chemistry is therefore necessary to derive constraints on $K_{yy}(\theta)$ and on advection in Jupiter's stratosphere at the mbar level. Such a model would also enable one to retrieve a reliable mass of the water that was initially deposited by the comet from these *Herschel* observations. Recent work by Dobrijevic et al. (2010, 2011) now enables reducing the size of chemical schemes to acceptable sizes to extend existing 1D photochemical models to 2D/3D by identifying key reactions in the more complete chemical schemes of 1D models. These reduced chemical schemes will facilitate the emergence of 2D/3D photochemical models because they reduce the computational time for chemistry by one to two orders of magnitude.

6. Conclusion

We have performed the first spatially resolved observations of water in the stratosphere of Jupiter with the HIFI and PACS instruments of the *Herschel* Space Observatory in 2009–2010 to determine its origin. In parallel, we monitored the stratospheric temperature in Jupiter with the NASA IRTF in the same periods to separate temperature from water variability in the *Herschel* maps.

We found that the shape of the water lines at 1669.9 GHz in the HIFI map recorded at very high spectral resolution proves that the bulk of water resides at pressures lower than 2 mbar. This rules out any steady source, like the IDP source, in which water would be present down to the condensation level (~20–30 mbar). A uniform source is also ruled out by both the HIFI and PACS maps. Indeed, the observations show a north-south asymmetry in the emission. The water column is roughly constant in the southern hemisphere and decreases linearly by a factor of 2–3 poleward in the northern hemisphere, at the spatial resolution of the observations. This distribution cannot be attributed to a hemispheric asymmetry in the stratospheric temperatures, according to our IRTF observations, but rather to meridional variability of the water column abundance. Thus, the spatial distribution of water in Jupiter's stratosphere is clear evidence that a recent comet, i.e., the Shoemaker-Levy 9 comet, is the principal source of water in Jupiter. What we observe today is a remnant of the oxygen delivery by the comet at 44 °S in July 1994.

It is possible that other sources like IDP or icy satellites may coexist at Jupiter, but, as demonstrated by this work, with other spatial distribution properties and lower magnitudes than the SL9 source. The upper limit derived for an IDP source by Lellouch et al. (2002) (with a flux of 8×10^4 cm^{-2} s^{-1}) is consistent with the *Herschel* observations, meaning that at least 95% of the observed water comes from the SL9 comet and subsequent (photo)-chemistry in Jupiter's stratosphere according to our models, as of today.

Although they reached their objective of determining the origin of the bulk of stratospheric water in Jupiter, the mapping observations we presented have insufficient latitudinal resolution and a lack of information at latitudes higher than ~60° to assess the relative magnitude of all possible water sources at Jupiter. The Submillimetre Wave Instrument (Hartogh et al. 2009a) is an instrument proposed for the payload of the recently selected Jupiter Icy Moon Explorer (JUICE), an L-class mission of the ESA Cosmic Vision 2015−2025 program, which is to be launched in 2022 and will study the Jovian system for 3.5 years starting in 2030. This instrument has several key objectives, one of which is to map in 3D SL9-derived species in the stratosphere of Jupiter with scale height vertical resolution and 1° resolution in latitude. It also proposes to measure the isotopic ratios in water and CO. The combination of these measurements will enable us to separate the spatial and isotopic signatures of all possible sources and their relative magnitude at Jupiter.

Acknowledgements. T. Cavalié wishes to thank J. Brillet for providing him with his baseline ripple removal tool for the purposes of this work. T. Cavalié acknowledges funding from the Centre National d'Études Spatiales (CNES). M. de Val-Borro acknowledges support from the Special Priority Program 1488 of the German Science Foundation, and grants NSF AST-1108686 and NASA NNX12AH91H. G. Orton acknowledges funding from the National Aeronautics and Space Administration to the Jet Propulsion Laboratory, California Institute of Technology. T. Greathouse acknowledges funding from NASA PAST grant NNX08AW33G and was supported as a Visiting Astronomer at the Infrared Telescope Facility, which is operated by the University of Hawaii under Cooperative Agreement no. NNX-08AE38A with the National Aeronautics and Space Administration, Science Mission Directorate, Planetary Astronomy Program. F. Billebaud wishes to thank the Programme National de Planétologie (PNP) of the Institut National des Sciences de l'Univers (INSU) for pluriannual funding on this project. HIFI has been designed and built by a consortium of institutes and university departments from across Europe, Canada and the United States under the leadership of SRON Netherlands Institute for Space Research, Groningen, The Netherlands and with major contributions from Germany, France and the US. Consortium members are: Canada: CSA, U.Waterloo; France: CESR, LAB, LERMA, IRAM; Germany: KOSMA, MPIfR, MPS; Ireland, NUI Maynooth; Italy: ASI, IFSI-INAF, Osservatorio Astrofisico di Arcetri-INAF; Netherlands: SRON, TUD; Poland: CAMK, CBK; Spain: Observatorio Astronómico Nacional (IGN), Centro de Astrobiología (CSIC-INTA). Sweden: Chalmers University of Technology – MC2, RSS & GARD; Onsala Space Observatory; Swedish National Space Board, Stockholm University – Stockholm Observatory; Switzerland: ETH Zurich, FHNW; USA: Caltech, JPL, NHSC. PACS has been developed by a consortium of institutes led by MPE (Germany) and including UVIE (Austria); KUL, CSL, IMEC (Belgium); CEA, OAMP (France); MPIA (Germany); IFSI, OAP/AOT, OAA/CAISMI, LENS, SISSA (Italy); IAC (Spain). This development has been supported by the funding agencies BMVIT (Austria), ESA-PRODEX (Belgium), CEA/CNES (France), DLR (Germany), ASI (Italy), and CICT/MCT (Spain). Data presented in this paper were analyzed using HIPE is a joint development by the *Herschel* Science Ground Segment Consortium, consisting of ESA, the NASA *Herschel* Science Center, and the HIFI, PACS and SPIRE consortia. This development has been supported by national funding agencies: CEA, CNES, CNRS (France); ASI (Italy); DLR (Germany). Additional funding support for some instrument activities has been provided by ESA. We are grateful to an anonymous referee for the constructive comments about this manuscript.

References

Bézard, B., Lellouch, E., Strobel, D., Maillard, J.-P., & Drossart, P. 2002, Icarus, 159, 95
Bjoraker, G. L., Stolovy, S. R., Herter, T. L., Gull, G. E., & Pirger, B. E. 1996, Icarus, 121, 411
Borysow, A., & Frommhold, L. 1986, ApJ, 304, 849
Borysow, J., Trafton, L., Frommhold, L., & Birnbaum, G. 1985, ApJ, 296, 644
Borysow, J., Frommhold, L., & Birnbaum, G. 1988, ApJ, 326, 509
Brown, L. R., & Plymate, C. 1996, J. Quant. Spec. Radiat. Transf., 56, 263
Cavalié, T., Billebaud, F., Biver, N., et al. 2008a, Planet. Space Sci., 56, 1573
Cavalié, T., Billebaud, F., Fouchet, T., et al. 2008b, A&A, 484, 555
Cavalié, T., Billebaud, F., Dobrijevic, M., et al. 2009, Icarus, 203, 531
Cavalié, T., Hartogh, P., Billebaud, F., et al. 2010, A&A, 510, A88
Cavalié, T., Biver, N., Hartogh, P., et al. 2012, Planet. Space Sci., 61, 3
Connerney, J. E. P. 1986, Geophys. Res. Lett., 13, 773
de Graauw, T., Helmich, F. P., Phillips, T. G., et al. 2010, A&A, 518, L6
Dobrijevic, M., Cavalié, T., Hébrard, E., et al. 2010, Planet. Space Sci., 58, 1555
Dobrijevic, M., Cavalié, T., & Billebaud, F. 2011, Icarus, 214, 275
Dutta, J. M., Jones, C. R., Goyette, T. M., & De Lucia, F. C. 1993, Icarus, 102, 232
Feuchtgruber, H., Lellouch, E., de Graauw, T., et al. 1997, Nature, 389, 159
Flasar, F. M. 1989, NASA Spec. Publ., 494, 324
Flasar, F. M., Kunde, V. G., Achterberg, R. K., et al. 2004, Nature, 427, 132
Fletcher, L. N., Orton, G. S., Yanamandra-Fisher, P., et al. 2009, Icarus, 200, 154
Fletcher, L. N., Orton, G. S., Rogers, J. H., et al. 2011, Icarus, 213, 564
Fouchet, T., Lellouch, E., Bézard, B., et al. 2000, A&A, 355, L13
Greathouse, T. K., Richter, M., Lacy, J., et al. 2011, Icarus, 214, 606
Griffith, C. A., Bézard, B., Greathouse, T., et al. 2004, Icarus, 170, 58
Hartogh, P., Barabash, S., Bolton, S., et al. 2009a, EPSC Abstracts, 4, EPSC2009
Hartogh, P., Lellouch, E., Crovisier, J., et al. 2009b, Planet. Space Sci., 57, 1596
Hartogh, P., Lellouch, E., Moreno, R., et al. 2011, A&A, 532, L2
Hesman, B. E., Davis, G. R., Matthews, H. E., & Orton, G. S. 2007, Icarus, 186, 342
Hueso, R., Wesley, A., Go, C., et al. 2010, ApJ, 721, L129
Kassis, M., Adams, J. D., Hora, J. L., Deutsch, L. K., & Tollestrup, E. V. 2008, PASP, 120, 1271
Lacy, J. H., Richter, M. J., Greathouse, T. K., Jaffe, D. T., & Zhu, Q. 2002, PASP, 114, 153
Landgraf, M., Liou, J.-C., Zook, H. A., & Grün, E. 2002, AJ, 123, 2857
Larson, H. P., Fink, U., Treffers, R., & Gautier, III, T. N. 1975, ApJ, 197, L137
Lellouch, E., Paubert, G., Moreno, R., et al. 1995, Nature, 373, 592
Lellouch, E., Bézard, B., Moses, J. I., et al. 2002, Icarus, 159, 112
Lellouch, E., Moreno, R., & Paubert, G. 2005, A&A, 430, L37
Lellouch, E., Bézard, B., Strobel, D. F., et al. 2006, Icarus, 184, 478
Lellouch, E., Hartogh, P., Feuchtgruber, H., et al. 2010, A&A, 518, L152
Leovy, C. B., Friedson, A. J., & Orton, G. S. 1991, Nature, 354, 380
Lomb, N. R. 1976, Ap&SS, 39, 447
Moreno, R., Marten, A., Matthews, H. E., & Biraud, Y. 2003, Planet. Space Sci., 51, 591
Moses, J. I., Lellouch, E., Bézard, B., et al. 2000, Icarus, 145, 166
Moses, J. I., Fouchet, T., Bézard, B., et al. 2005, J. Geophys. Res., 110, 8001
Niemann, H. B., Atreya, S. K., Carignan, G. R., et al. 1998, J. Geophys. Res., 103, 22831
Orton, G. S., Friedson, A. J., Caldwell, J., et al. 1991, Science, 252, 537
Orton, G. S., Fletcher, L. N., Lisse, C. M., et al. 2011, Icarus, 211, 587
Ott, S. 2010, in Astronomical Data Analysis Software and Systems XIX, eds. Y. Mizumoto, K.-I. Morita, & M. Ohishi, PASP, 434, 139
Pickett, H. M., Poynter, I. R. L., Cohen, E. A., et al. 1998, J. Quant. Spectr. Rad. Trans., 60, 883
Pilbratt, G. L., Riedinger, J. R., Passvogel, T., et al. 2010, A&A, 518, L1
Poglitsch, A., Waelkens, C., Geis, N., et al. 2010, A&A, 518, L2
Prather, M. J., Logan, J. A., & McElroy, M. B. 1978, ApJ, 223, 1072
Roelfsema, P. R., Helmich, F. P., Teyssier, D., et al. 2012, A&A, 537, A17
Rothman, L. S., Rinsland, C. P., Goldman, A., et al. 1998, J. Quant. Spectr. Rad. Trans., 60, 665
Sánchez-Lavega, A., Wesley, A., Orton, G., et al. 2010, ApJ, 715, L155
Selsis, F., Brillet, J., & Rapaport, M. 2004, A&A, 416, 783
Strobel, D. F., & Yung, Y. L. 1979, Icarus, 37, 256
Wong, M. H., Mahaffy, P. R., Atreya, S. K., Niemann, H. B., & Owen, T. C. 2004, Icarus, 171, 153

Pages 15 to 16 are available in the electronic edition of the journal at http://www.aanda.org

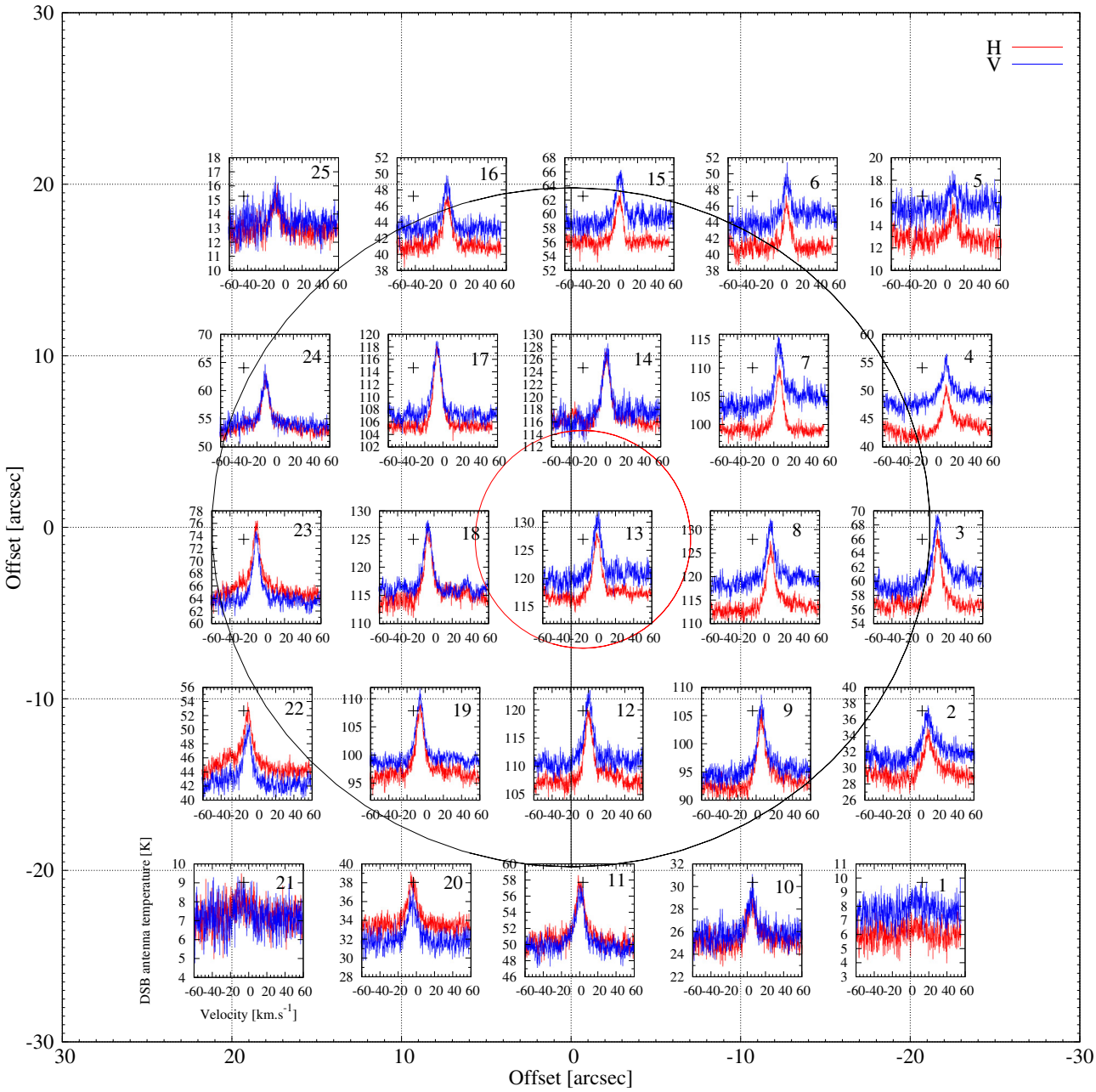

Fig. 1. Water 5×5 raster map at 1669.9 GHz obtained with *Herschel*/HIFI on July 7, 2010, after reducing the raw data with the HIPE 8.2.0 pipeline. The data are shown at their native resolution (1.1 MHz). The pixels are numbered according to the raster observation numbering. The H (red line) and the V (blue line) polarizations of the WBS are both presented. Jupiter is represented with the black ellipse, and its rotation axis is also displayed. The black crosses indicate the center of the various pixels according to the H/V mean positions retrieved from the modeling of the continuum emission. The beam is represented for the central pixel by the red circle.

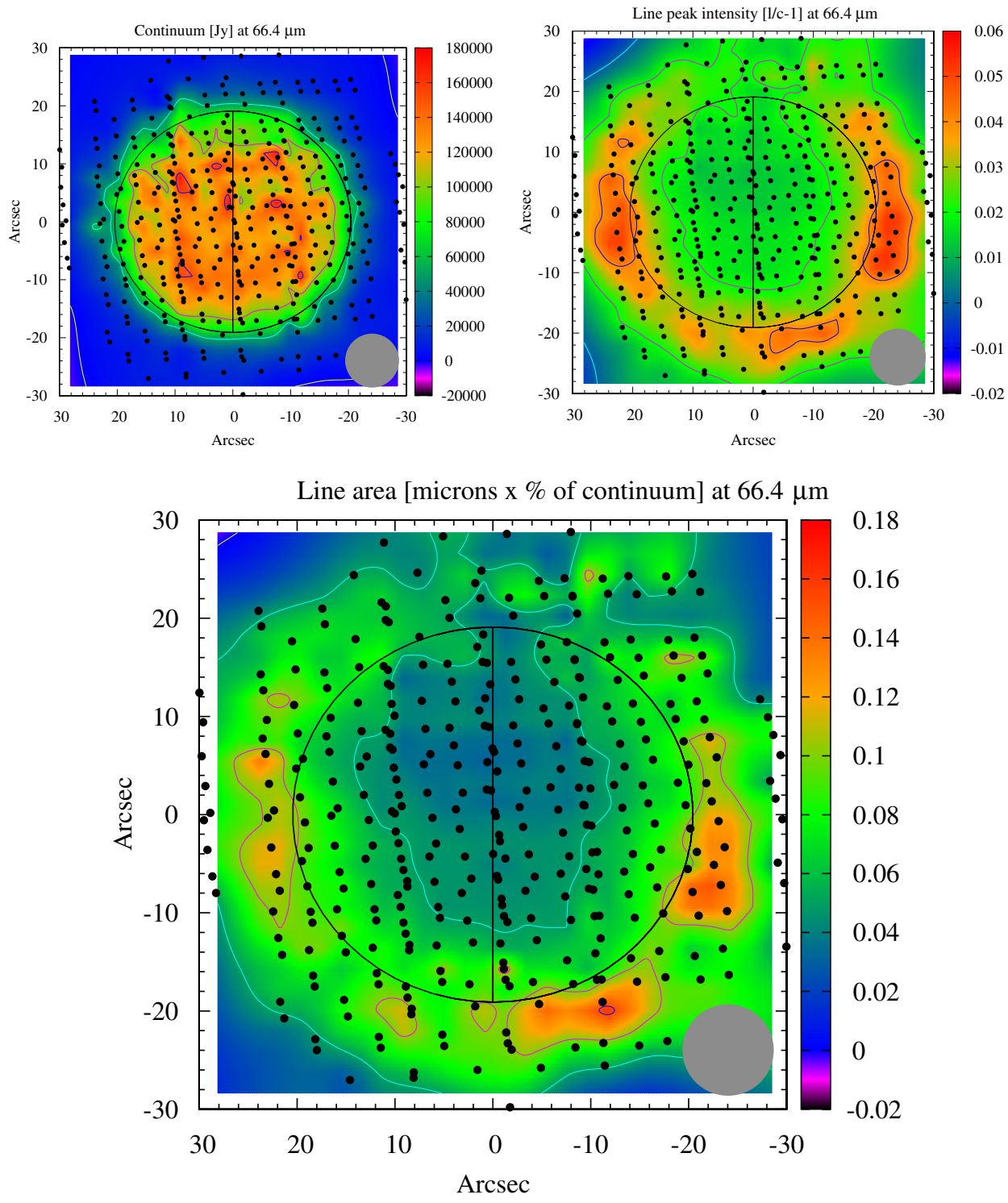

Fig. 3. Water map at 66.4 μm observed by the PACS spectrometer on December 15, 2010. Jupiter is represented by the black ellipse, and its rotation axis is also displayed. The beam is represented by a gray filled circle. The continuum (in Jy), the line peak intensity (=l/c-1), and the line area (in microns × % of the continuum) are displayed. While the line peak intensity and line area values can be relied on, the absolute flux values cannot (see text for more details). This map confirms the lack of emission at mid-to-high latitudes in the northern hemisphere (best seen at the limb).